Nuclear Science and Techniques (2025) 36:114
https://doi.org/10.1007/s41365-025-01668-6

Single-neutron super-resolution imaging based on neutron capture event detection and reconstruction

Yu-Hua Ma[1,2] · Bin Tang[1] · Wei Yin[1] · Hang Li[1] · Hong-Wen Huang[1] · Hong-Li Chen[2] · Xin Yang[1] · He-Yong Huo[1] · Yong Sun[1] · Sheng Wang[1] · Bin Liu[1] · Run-Dong Li[1] · Yang Wu[1]

Received: 17 April 2024 / Revised: 17 April 2024 / Accepted: 18 May 2024 / Published online: 7 May 2025

Abstract

Neutron capture event imaging is a novel technique that has the potential to substantially enhance the resolution of existing imaging systems. This study provides a measurement method for neutron capture event distribution along with multiple reconstruction methods for super-resolution imaging. The proposed technology reduces the point-spread function of an imaging system through single-neutron detection and event reconstruction, thereby significantly improving imaging resolution. A single-neutron detection experiment was conducted using a highly practical and efficient ^{6}LiF-ZnS scintillation screen of a cold neutron imaging device in the research reactor. In milliseconds of exposure time, a large number of weak light clusters and their distribution in the scintillation screen were recorded frame by frame, to complete single-neutron detection. Several reconstruction algorithms were proposed for the calculations. The location of neutron capture was calculated using several processing methods such as noise removal, filtering, spot segmentation, contour analysis, and local positioning. The proposed algorithm achieved a higher imaging resolution and faster reconstruction speed, and single-neutron super-resolution imaging was realized by combining single-neutron detection experiments and reconstruction calculations. The results show that the resolution of the 100 μm thick ^{6}LiF-ZnS scintillation screen can be improved from 125 to 40 microns. This indicates that the proposed single-neutron detection and calculation method is effective and can significantly improve imaging resolution.

Keywords Neutron capture reaction · Super-resolution imaging · Weak light detection · Event reconstruction

1 Introduction

With the development of neutron sources and advances in neutron detection [1–4], neutron imaging has attained exceptional spatial and temporal resolution, rendering it applicable across numerous fields [5–7]. Currently, advanced imaging methods and detection technologies have been emerging one after another [8–14], including various neutron scintillation screens, scintillating fibers, charge coupled device/complementary metal-oxide semiconductor (CCD/CMOS), neutron imaging plates (NIP), and other key imaging devices with advanced performance [15–20]. This has made it difficult to physically modify imaging instruments and improve the resolution of imaging systems. However, with the continuous development of technology, the demand for higher detection accuracy and more precise target detection is increasing, prompting neutron imaging technology to move toward higher resolutions.

This work was supported by the National Natural Science Foundation of China (Nos. 12205271, 12075217, U20B2011, and 51978218), Sichuan Science and Technology Program (No. 2019ZDZX0010), and the National Key R&D Program of China (No. 2022YFA1604002).

✉ Wei Yin
yinwei-itm@163.com

✉ Hang Li
lihang32@gmail.com

✉ Hong-Wen Huang
hhw@caep.cn

✉ Hong-Li Chen
hlchen1@ustc.edu.cn

[1] Chinese Academy of Engineering Physics, Mianyang 621000, China

[2] University of Science and Technology of China, Hefei 230026, China

Typically, a neutron imaging detection system consists of a neutron scintillation screen, mirror, lens group, CCD, or CMOS [21–25]. The conclusions drawn from modern information optics theory indicate that in a spatially invariant linear system, any imaging device is equivalent to a filter in space. These devices contribute to point diffusion and blurred images. Among these, the blurring effect of the scintillation screen is critical [26, 27]. Inside the scintillation screen, neutrons react with neutron converters such as ^{6LiF}, whereby particle transport and fluorescence transport occur. These transport processes contribute to a strong point-spread effect in imaging [28]. Neutron scintillation screens have become the main factor restricting imaging resolution and are a key component in improving the quality of neutron imaging [29].

Research on improving the resolution of imaging systems is relatively mature [30]. Current research covers device characteristics and various imaging techniques in terms of hardware [31–34] and diverse image processing methods in computation [5, 35–37]. Existing research mainly focuses on high-resolution thin screens (50 µm ^{6}LiF-ZnS, thinner Gd_2O_2S screens [38, 39]), or doped (Gd/B) neutron-sensitive microchannel plates (MCP) [40]. Single-neutron detection and reconstruction is a novel experimental imaging method that can obtain high-resolution neutron images without changing the original device, which is a highly meaningful technical route.

This study explores a super-resolution imaging method based on single-neutron detection and reconstruction. This method can detect single neutrons and remove the blur caused by point diffusion based on a specific measurement method proposed for neutron capture events in experimental detection and an inexpensive widely used ^{6}LiF-ZnS scintillation screen (100 µm) to complete the experimental measurement of the reactor. Four reconstruction algorithms were proposed for this computation. The proposed method not only effectively extracts signals and distinguishes noise to further improve resolution but also reduces computational complexity and improves reconstruction speed.

2 Materials and methods

2.1 Theory

In neutron radiography, incident neutrons react with ^{6}LiF in the scintillation screen and emit ZnS fluorescence. Conventional imaging is typically achieved through exposure to scintillation screens, integrating the fluorescence distribution $I(t, s)$ over time, as follows:

$$I(s) = \int_{\text{Exposure-time}} I(t,s)\mathrm{d}t \tag{1}$$

where $I(t)$ represents the light intensity distribution in the image; s is the spatial position; and t is exposure time.

This work achieved single-neutron detection by detecting the fluorescence spots generated by neutron reactions individually, subsequently calculating the precise position of the incident neutron using a reconstruction algorithm. Using a dot with a precise location to replace the fluorescent Airy spot (light clusters), point diffusion and blurring during imaging can be reduced. Finally, a large number of light-dot distributions are added to form a higher-resolution neutron image.

Theoretically, single-neutron detection is equivalent to the time differential of the photon distribution $I(t, s)\mathrm{d}t$. If the light-dot distributions are directly superimposed, the resulting image is equivalent to traditional imaging $\int I(t, s)\mathrm{d}t$. If they are superimposed after reconstructing $P(I(t, s)\mathrm{d}t)$, super-resolution imaging can be achieved.

$$I^{\mathrm{HR}}(s) = \int_{\text{All-exposure-time}} P[I(t,s)]\mathrm{d}t \tag{2}$$

where $I^{\mathrm{HR}}(s)$ represents the high-resolution image, and $P(\cdot)$ represents the reconstruction process.

Although this method can effectively achieve super-resolution imaging, it also places higher requirements on detection technology and the reconstruction algorithm. To detect a single event experimentally, the detection system must obtain a distinguishable weak light signal under intrinsic noise. During computations, each event in each frame is extracted and calculated. Considering the substantial computational resources and time required by the large number of neutron events, the efficiency of the algorithm should be improved. For weak light sources, the main problems are experimental detection and positioning calculations, making it critical to distinguish between noise and weak light signals. Thus, algorithms still need to improve noise discrimination.

2.2 Experiment

The most basic task accomplished in this experiment was to detect a single-neutron event. Measuring each neutron radiation capture event under a continuous neutron beam requires individual measurements of the fluorescence produced by the event and its spatial distribution. The spatial distribution of fluorescence is the basis of traditional and super-resolution imaging. The fluorescence distribution can be directly superimposed during data processing to obtain an image, equivalent to that of conventional integral imaging.

Alternatively, the detection results for single neutrons can be processed to achieve super-resolution imaging.

The guiding principle of the experiment was single-neutron detection and reconstruction, as shown in Fig. 1. (I) In Fig. 1a, traditional imaging detects all the neutrons during a single exposure, which is equivalent to time integration. Each Gaussian-like spot overlaps with the others, eventually forming an image with a blurred result. (II) In Fig. 1b, single-neutron detection aims to detect neutrons individually, to obtain individual spot distributions. If reconstruction is not performed, all spots that directly overlap are equivalent to those in the traditional imaging method. (III) In Fig. 1c, single-neutron super-resolution imaging aims to reconstruct the precise position of each neutron event, spot by spot. By superimposing the reconstructed points with small-scale distribution (pixel level), the spatial resolution of the imaging can be significantly improved.

The measurements were conducted at a Cold Neutron Radiography Facility (CNRF) located at the C1 beam tube of the China Mianyang Research Reactor (CMRR). The neutrons emitted from the C1 beam tube have a cold neutron spectrum with a characteristic wavelength of 0.26 nm (approximately 0.121 eV). The neutron flux can reach $3.41 \times 10^8 \mathrm{cm}^{-2}\mathrm{s}^{-1}$, and the neutron flux at the sample position can reach $8 \times 10^6 \mathrm{cm}^{-2}\mathrm{s}^{-1}$ [41]. Various collimation ratios (tube lengths and aperture sizes) were available, and the aperture size used in this study was ϕ 10 cm. The main components of the neutron imaging instrument include a ^{6}LiF-ZnS scintillator screen, mirror, optical lens group, image intensifier, and sCMOS camera. The CNRF facility and its imaging system are shown in Fig. 2 [42].

The ^{6}LiF-ZnS scintillation screen used in CNRF is also the most widely used and cost-effective neutron scintillation screen. Aluminum with a small cross-section was used as the base material of the scintillator screen, coated with a scintillator material thickness of 100 µm. The scintillator screen was composed of neutron converter material ^{6}LiF, fluorescent material ZnS(Ag), and binder epoxy resin at a mass ratio of 1:2:1.29. The overall density was 2.845 g/cm^3. The typical size of ^{6}LiF and ZnS particles is approximately 1.5 µm–5 µm. The characteristic wavelength of the fluorescence spectrum was 450 nm, and fluorescence decay time was 200 ns.

The camera used was an ANDOR iStar-sCMOS, which provides high-resolution and high frame rate measurements. This camera can capture 12-bit or 16-bit images with an image array size of 2560 × 2560. The camera read images at a frame rate of 50 fps with full-frame resolution and 16 bit depth. An MCP was installed in the iStar-sCMOS camera as an image intensifier, which provided a maximum gain of 4096 times. This facilitates the detection of weak fluorescence. MCP has a peak quantum efficiency (QE) of up to 50 % and spectral coverage of 120 to 1100 nm. MCP uses P46 phosphor with a light decay time of 200 ns (2 ms for P43), which is the main limitation to the optical interframe time (300 ns). The optical resolution

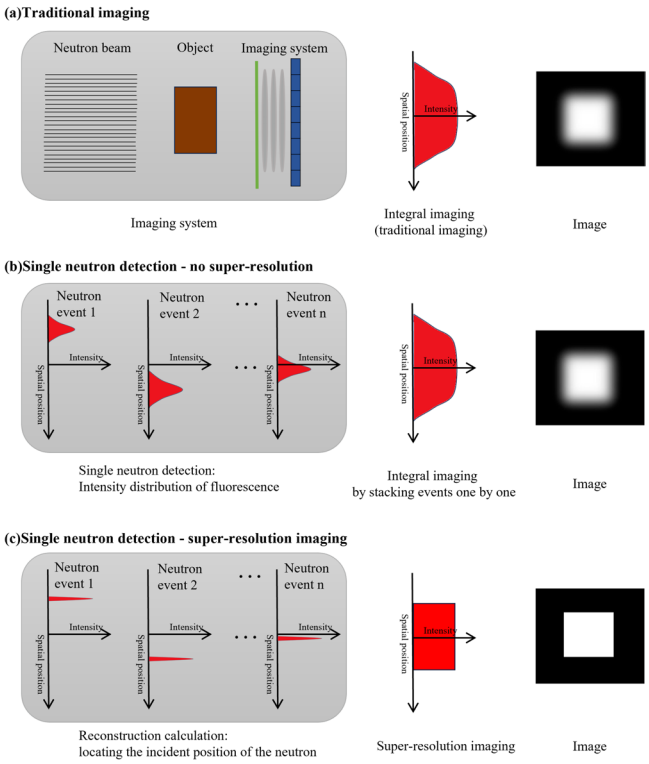

Fig. 1 (Color online) Imaging method sketch: (**a**) integral imaging (traditional imaging method); (**b**) integral imaging based on single-neutron detection; and (**c**) super-resolution imaging based on single-neutron detection

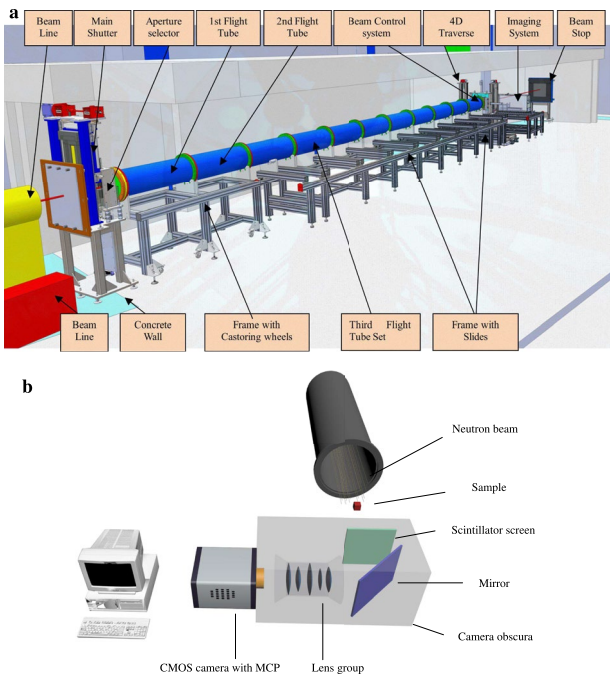

Fig. 2 (Color online) Experimental setup (**a**) Sketch of Cold Neutron Radiography Facility and (**b**) sketch of imaging system at CNRF

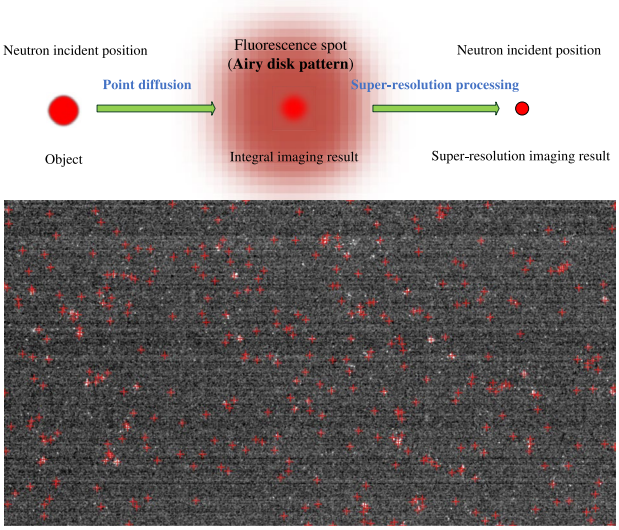

Fig. 3 (Color online) Sketch of reconstruction principle

limit of the MCP (P46 phosphor) produced by Andor was 35 μm.

When collecting images, the field of view size was adjusted to 27 mm×27 mm to cover the entire sample. The sample used was a gadolinium resolution grating manufactured by the Paul Scherrer Institute. To minimize blurring caused by beam divergence, a resolution grating was placed close to the detector. The gain of MCP was set to 2000. The detector acquired images at a resolution of 2560×2560 pixels and read out a region of interest of 2560×1360 pixels at a higher detection frame rate. The acquisition was conducted in 12 bit low-noise mode. To detect the light spots generated by single neutrons and avoid the stacking of light spots as much as possible, the exposure time of the detector was set to 2 ms. After cooling the camera sensor to 0 °C, 190 thousand images were collected. Once the test was completed, the beam aperture was closed, and five thousand dark field images were acquired for noise removal.

2.3 Reconstruction method

Theoretically, each interaction on the scintillation screen material produces a star-shaped spot of light. In this experiment, the light spots produced by each capture reaction were recorded under a very short exposure time (millisecond). During reconstruction, the position of each light spot was calculated, and a value was assigned to the corresponding pixel. Reconstructing each nuclear event for each frame and eventually stacking all the frames enables high-resolution imaging. Each reconstruction calculation was performed for a single event, whereby the imaging technique transformed from a frame-based to an event-based system.

In single-neutron super-resolution imaging, the key steps of the reconstruction algorithm are as follows: (i) processing image noise and extracting fluorescence signals and (ii) calculating the location of neutron capture events and reducing the point diffusion effect produced by the imaging device. Combining single-neutron detection with reconstruction enabled super-resolution imaging. A schematic representation of this principle is shown in Fig. 3.

In this study, four advanced algorithms are proposed, and their reconstruction results are presented. The first is an improved centroid algorithm based on the existing algorithm, and the rest are the median filter centroid, median filter extremum, and Gaussian filter extremum algorithms. A schematic of the calculation process is presented in Fig. 4. Compared with the existing centroid algorithm (Fig. 4a), these algorithms offer additional advantages in terms of noise discrimination, and the calculated reconstructed images are more credible.

The calculation steps of the centroid algorithm (Fig. 4b) entail subtracting the background noise, spot segmentation, contour morphology analysis, and centroid calculation. In denoising, the image measured in the dark field can be removed as fixed noise, leaving only random noise. In spot segmentation, a threshold is set to eliminate random noise and low signal-to-noise ratio (SNR) light spot signals, and each spot area is segmented and processed. In contour analysis, the position, area, perimeter, and other morphological features of the contour are determined, and the relationship

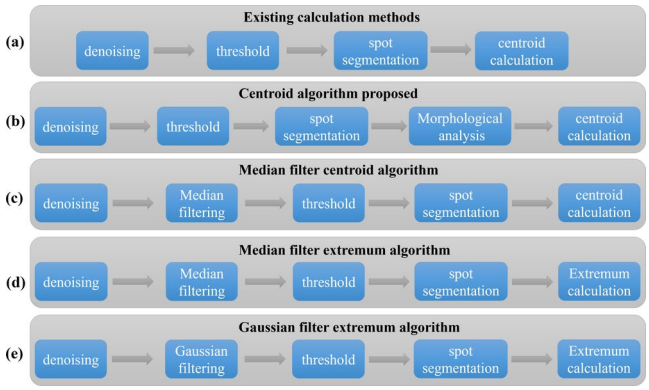

Fig. 4 (Color online) Sketch of the reconstruction algorithm

between the parent and child contours is established. In centroid calculation, the area and circumference of the contour can be considered as the condition for removing the low SNR signals. The centroid position of the light spot is then calculated to obtain a high-resolution image. Compared with the traditional method, which directly calculates the spot centroid, this method can remove noise more thoroughly and reconstruct a super-resolution image with higher credibility.

The median filter centroid algorithm is similar to the centroid algorithm (Fig. 4c). The difference is that a median filter is added after subtracting the background noise, and the filter kernel covers a radius of three pixels. The random noise in the image is close to the gray value signal and similar to the peak-shaped signal. However, the noise distribution range is smaller. Median filtering eliminates random noise that is similar to the signal. The advantage of median filtering is that it can remove noise with less signal loss. However, the disadvantages are that it changes the signal distribution and flattens the peak of the spot, which can change the centroid position.

The median filter extremum and Gaussian filter extremum algorithms are faster reconstruction methods (Fig. 4d and 4e). The calculation steps of these two algorithms include background subtraction, median/Gaussian filtering, spot segmentation, and local extreme-value calculation. Compared with the centroid algorithm, the extremum algorithm has less computation, faster reconstruction speed, and a better noise reduction effect.

The addition of the median and Gaussian filtering operations can solve these two problems. First, for the amount of data (a large number of images x hundreds of light spots), the faster algorithm clearly has more potential for development. Direct filtering of the entire image is faster than analyzing the morphological characteristics of the light spots individually. In addition, in weak light detection, such as neutron event imaging, noise elimination is an important task. Although weak noise with low gray values can be removed by thresholding, noise with large gray values in small areas (compared to gray signal areas) still remains in weak light detection. Removing this signal-like noise using a centroid algorithm is difficult. However, the operation of filtering and threshold combination can eliminate the noise with large gray values in small areas, to better distinguish between noise and signal. Compared with median filtering, Gaussian filtering can reduce the gray value of noise to a greater extent and further enhance the signal–noise discrimination ability.

The addition of median and Gaussian filtering operations can solve these two problems. First, for the amount of data (a large number of images × hundreds of light spots), the faster algorithm clearly has more potential for development. Directly filtering the entire image is faster than analyzing the morphological characteristics of the light spots individually. In addition, in weak light detection, such as neutron event imaging, noise elimination is an important task. Although weak noise with low gray values can be removed by thresholding, noise with large gray values in small areas (compared to gray signal areas) remains in weak light detection. Removing this signal-like noise using a centroid algorithm is difficult. However, the operation of filtering and threshold combination can eliminate the noise with large gray values in small areas and further enhance the signal–noise discrimination ability.

3 Results and discussion

3.1 Experimental results and evaluation

For the reactor power near 10 MW, 1.9×10^5 images and 5×10^3 background images were collected at approximately 1.3 Tb. The original images are shown in Fig. 5. The raw data contained light spots produced by neutron capture events, as well as a large amount of noise. The image noise obtained by the CMOS sensor is mainly divided into random and fixed-pattern noise.

The fixed-pattern noise is primarily caused by the reset voltage deviation, which, in turn, is caused by factors such as

Fig. 5 Raw image data

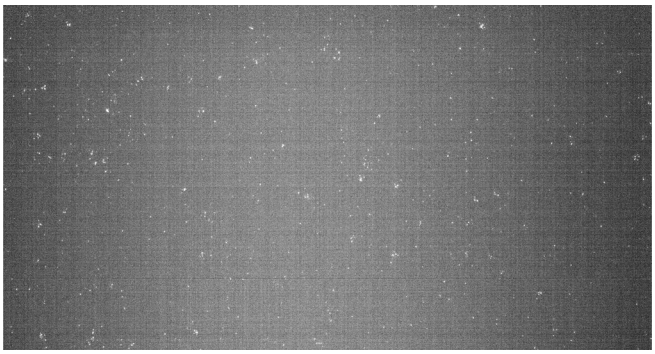

the metal-oxide semiconductor field-effect transistor (MOS FET) threshold voltage deviation in the pixel, gain deviation of the source follower, and gain and bias of the column amplifier. This is a type of non-transient spatial noise. Therefore, it can be eliminated by using a multiframe averaging method. The average noise value of 5000 background images can be used to eliminate the fixed-pattern noise to a certain extent.

The numerous sources of random noise include power voltage fluctuations, substrate coupling between CMOS sensors and peripheral devices, and reset and readout processes of pixel transistors, which mainly comprise dark current, transfer, reset, flicker (1/*f*), and shot noise. The spatial distribution of random noise is not fixed; therefore, its direct removal is difficult. However, it can be distinguished based on the gray value and contour features during reconstruction. The morphological analysis link in the centroid algorithm (Fig. 4b) was used to analyze the area, perimeter, shape, and other characteristics of the light spot.

Comparing the effects of neutron event imaging requires the results of traditional integral imaging. By subtracting the multiframe background average from the original image data and then setting a threshold to remove the noise with low gray value, integral imaging was performed with 2 ms exposure. The traditional integral imaging results were obtained by superimposing 1.9×10^5 frames, as shown in Fig. 6, where the 125 μm stripes of the resolution grating are clearly visible at a field of view of 2.7 cm ×2.7 cm. There are four easily distinguishable peaks in the grayscale distribution map. The 100 μm stripes are difficult for the human eye to distinguish. With four peaks, the gray distribution is not ideal. Therefore, the resolution of the conventional method is considered to be 125 μm and barely 100 μm.

In image reconstruction, the centroid, median filter centroid, median filter extremum, and Gaussian filter extremum algorithms were used to calculate the positions of neutron capture occurrence events in 1.9×10^5 images. High-resolution images were obtained. The results of the super-resolution experiments are shown in Fig. 7. After analyzing, the spatial resolution of the super-resolution image was significantly improved, and the results are shown in Table 1.

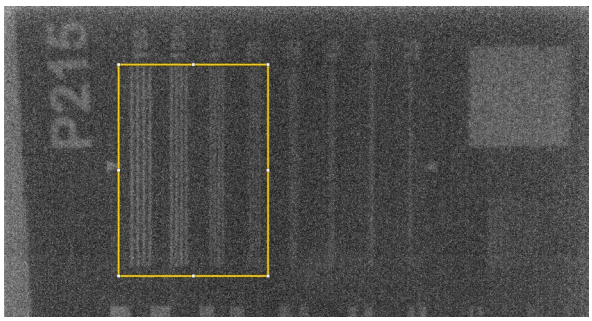

(a) Neutron image.

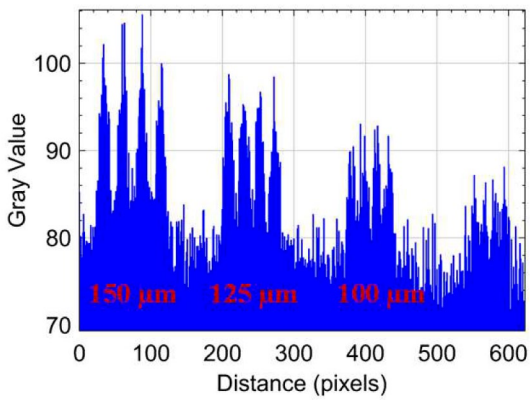

(b) Grayscale distribution of ROI in sCMOS image.

Fig. 6 (Color online) Traditional integral imaging and its resolution level

To more accurately evaluate the super-resolution effect of single-neutron imaging, the image can be evaluated subjectively. From an objective aspect, line pair gray analysis and modulation transfer function were used to evaluate the resolution improvement effect.

The reconstruction results of the centroid algorithm shown in Fig. 7a and b can achieve a resolution of 50 μm. In the gray analysis, 50 μm stripes can be clearly distinguished, whereas 40 μm stripes cannot be distinguished.

The median filtering centroid algorithm in Fig. 7c and d and median filtering extremum algorithm in Fig. 7e and (f) have similar effects. Both algorithms can achieve resolutions

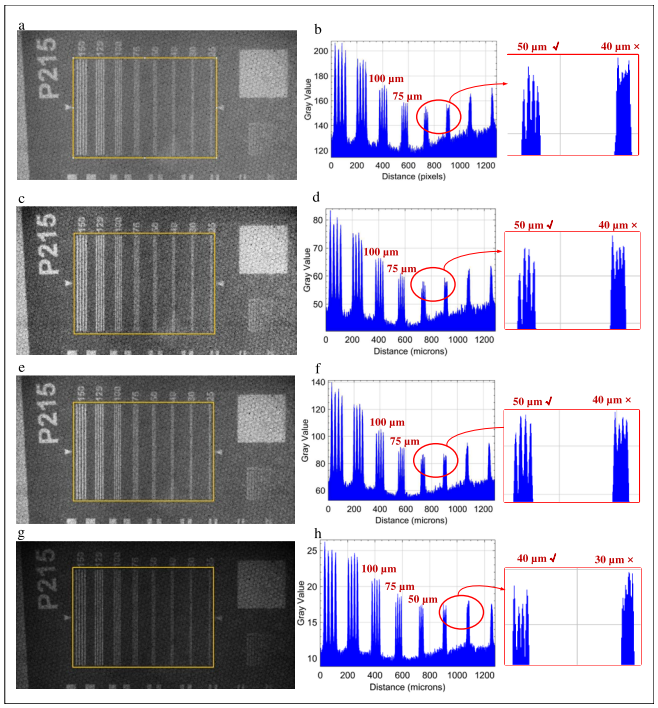

Fig. 7 (Color online) Super-resolution reconstruction results and grayscale distribution of resolution fringes. **a** Reconstruction results of the centroid algorithm; **b**)Distribution of resolution fringes calculated by centroid algorithm; **c** Reconstruction results of median filter centroid algorithm; **d** Distribution of resolution fringes calculated by median filter centroid algorithm; **e** Reconstruction results of median filter extremum algorithm; **f** Distribution of resolution fringes calculated by median filter extremum algorithm; **g** Reconstruction results of Gaussian filter extremum algorithm; and **h** Distribution of resolution fringes calculated by Gaussian filter extremum algorithm

Table 1 Super-resolution experimental results

	Traditional imaging (original image)	Single-neutron imaging (super-resolution image)			
		Centroid algorithm	Median filtering centroid algorithm	Median filtering extremum algorithm	Gaussian filter extremum algorithm
Spatial resolution (μm)	100–125	50	40–50	40–50	40

between 50 μm and 40 μm. In grayscale analysis, the 50 μm stripes can be clearly distinguished, whereas the 40 μm stripes can barely be distinguished. This improvement in resolution indicates that median filtering can eliminate random noise. Because median filtering changes the signal distribution, it can further reduce the effect of noise on neutron event discrimination. In addition, the extremum algorithm has a faster reconstruction speed (in this experiment, five times that of the centroid algorithm).

According to the reconstruction results in Fig. 7g and (h), the Gaussian filter extremum algorithm can achieve a resolution of 40 μm. The Gaussian filter extremum algorithm obtained the best resolution and fastest reconstruction by virtue of its excellent random noise reduction and an ability to maintain constant peaks.

After comparing various algorithms, the results show that the Gaussian filter extreme-value algorithm has the best effect, as reflected by the optimal resolution level. The reconstructed image quality has higher clarity and better subjective visualization. In addition, it has the advantages of a small number of calculations and high speed.

The modulation transfer function (MTF) is an important optical system evaluation indicator and can be used to calculate the resolution. Although the method of observing line pairs is the most direct and reliable, MTF can still be used as an additional method for verification.

An edge-to-edge method was selected for the calculation of the MTF curves. In terms of calculation objects, given the excellent performance of the Gaussian filter extremum algorithm, its reconstructed image was used as the representative of super-resolution. The MTF curves of the original and super-resolution images are compared in Fig. 8. The image resolutions calculated from the curves at 50 % and 10 % MTF are shown in Table 2.

At the same MTF, the super-resolution image had higher-frequency line pairs, such that the resolution level was also higher. The resolution obtained at 50 % MTF, which corresponds to the most sensitive human eye, was 41.7 μm. The resolution obtained by directly observing the grayscale distribution of the line pairs with the human eye was 40 μm. Regardless of observing line pairs or analyzing MTF to assess resolution, the final results demonstrate that the experimental approach and reconstruction algorithm for single-neutron imaging are solutions that effectively improve imaging resolution.

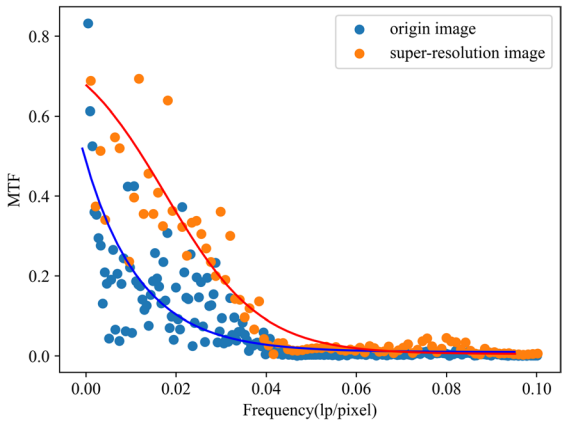

Fig. 8 (Color online) MTF curves of the original and super-resolution images

Table 2 Resolution size under different discrimination conditions

Data	Grayscale analysis of line pairs (μm)	50 % MTF (μm)	10 % MTF (μm)
Origin image	125	375.1	21.2
Super-resolution images	40	41.7	12

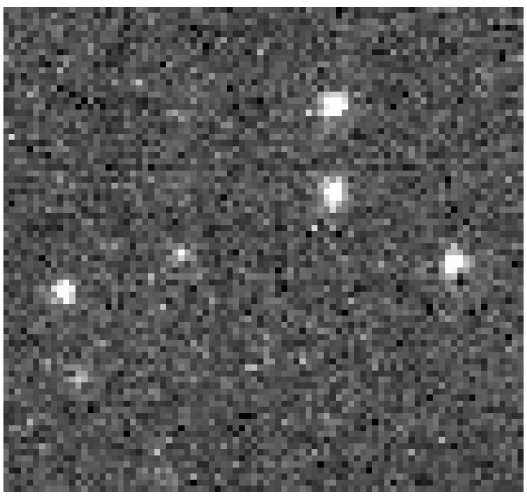

Fig. 9 (Color online) A small area of raw image data (86 × 80 pixels)

3.2 Algorithm feature mining

To more concretely demonstrate the functions and characteristics of the algorithm, a small area with a high signal-to-noise ratio was intercepted from the original image for independent calculations, as shown in Fig. 9.

The specific calculation steps and processing effects of the centroid algorithm are illustrated in Fig. 10. (I) Most

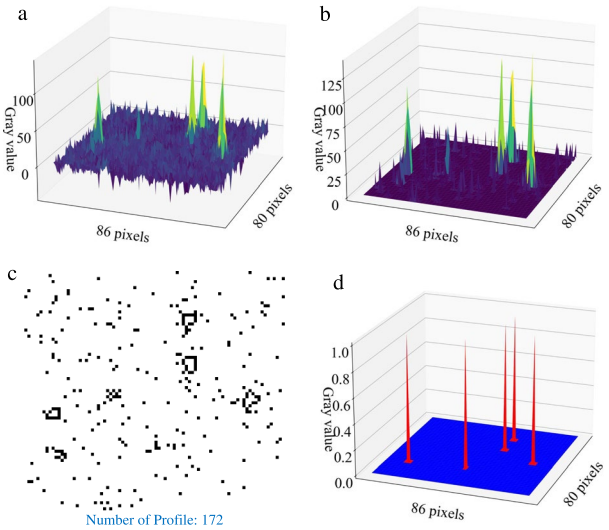

Fig. 10 (Color online) Centroid algorithm: (**a**) grayscale distribution of original data; (**b**) grayscale distribution after spot segmentation; (**c**) contour line of light spot; and (**d**) grayscale distribution of reconstruction results

of the random noise in Fig. 10a can be removed by setting threshold segmentation spots. However, according to Fig. 10b, noisy areas with high gray values remain, and the threshold cannot be further increased to remove noise to minimize the loss of the neutron signal. (II) Contour feature discrimination is a feasible method for further processing. The contour features are calculated using Suzuki85 boundary tracking algorithm, as shown in Fig. 10c. (III) Neutron signals can be filtered out based on contour features to obtain the distribution of the pixel positions where the neutron signals are located, as shown in Fig. 10d.

The centroid algorithm can analyze light spots individually and perform processing based on the shape, area, perimeter, and other image moment information. The centroid algorithm has many adjustable parameters, including the threshold and spot image moment parameters. However, the disadvantage is that the effect of noise elimination is poor, and the amount of calculation is large.

The Gaussian filter algorithm can improve the resolution from 125 μm to 40 μm. To more concretely demonstrate the functions and characteristics of the algorithm, the intermediate calculation results are shown in Fig. 11. Through Gaussian filtering, the random noise in Fig. 11a is reduced and smoothed, to obtain the result in Fig. 11b. The distribution of light spots with low SNR and random noise is generally smaller. Gaussian filtering can significantly reduce the grayscale for a better filtering effect. Therefore, setting a lower threshold after Gaussian filtering can effectively segment the signal spots as shown in Fig. 11c. Finally, the single-pixel distribution of the neutron signal was reconstructed, as shown in Fig. 11d.

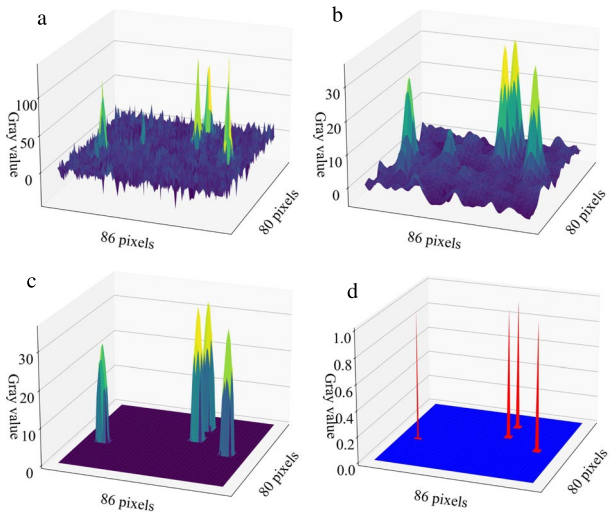

Fig. 11 (Color online) Gaussian filter algorithm: grayscale distribution of (**a**) original data; (**b**) after filtering; (**c**) after spot segmentation; and (**d**) reconstruction results

Gaussian filtering algorithms not only have a stronger signal-to-noise screening capability but also are faster. In addition, the algorithm can flexibly adjust the array size of the Gaussian filter kernel, sigma value, and spot segmentation threshold. These variable parameters enable the algorithm to remain well adapted under different experimental conditions, ensuring effective screening of neutron signals and noise.

4 Conclusion

This study demonstrates the principle of super-resolution imaging based on neutron capture events. A super-resolution imaging instrument was installed at the cold neutron source of the CMRR. Commonly used ^{6}LiF-ZnS scintillation screens, MCP and CMOS, were used for the hardware. The weak light signal produced by the neutron capture event was successfully detected, and super-resolution imaging was achieved using a reconstruction algorithm.

Super-resolution imaging based on neutron capture events requires the processing of a large amount of image data; therefore, the computing time is an important factor. The median filtering extremum and Gaussian filtering extremum algorithms proposed in this study process pixel clusters frame by frame rather than individually. The reconstruction speeds of these two methods are higher. In addition, super-resolution imaging makes it crucial to deal with the noise generated by MCP and CMOS. The Gaussian filter extremum algorithm can effectively distinguish between signals and noise, reducing signal loss without changing the peak position of the light spot. In this experiment, the resolution was improved from 125 μm to 40 μm, which is an improvement of 68 %.

This work provides both experimental and computational solutions and proves that these solutions perform better methodologically. A better resolution can be achieved with a smaller field of view, thinner Gd_2O_2S scintillation screen, and smaller MCP aperture. Neutron super-resolution imaging can significantly improve spatial resolution, which is attractive for many studies with non-destructive testing requirements. Non-destructive high-resolution testing will also promote further research and applications.

Author contributions All authors contributed to the study conception and design. Material preparation, data collection, and analysis were performed by Bin Tang, Wei Yin, and Yu-Hua Ma. The first draft of the manuscript was written by Yu-Hua Ma, and all authors commented on the previous versions of the manuscript. Institutions are ranked alphabetically, and all share a joint first rank with equal contribution. All authors read and approved the final manuscript.

Data availability The data that support the findings of this study are openly available in Science Data Bank at https://cstr.cn/31253.11.sciencedb.j00186.00547 and https://www.doi.org/10.57760/sciencedb.j00186.00547 .

Declarations

Conflict of interest The authors declare that they have no conflict of interest.

References

1. R. He, X.Y. Niu, Y. Wang et al., Advances in nuclear detection and readout techniques. Nucl. Sci. Tech. **34**, 205 (2023). https://doi.org/10.1007/s41365-023-01359-0
2. J. Dumazert, R. Coulon, Q. Lecomte et al., Gadolinium for neutron detection in current nuclear instrumentation research: A review. Nucl. Instrum. Meth. Sect. A **882**, 53–68 (2018). https://doi.org/10.1016/j.nima.2017.11.032
3. E. Lehmann, Status and progress in neutron imaging detection systems. IAEA-TECDOC. Vienna: IAEA 261-271 (2020). https://inis.iaea.org/search/search.aspx?orig-q=RN:52019820
4. L.F. He, S.B. Han, G.H. Wei et al., Development and application of neutron imaging technique at China Advanced Research Reactor. Mater. Sci. Forum **850**, 153–160 (2016). https://doi.org/10.4028/www.scientific.net/MSF.850.153
5. D.K. Aswal, P.S. Sarkar, Y.S. Kashyap, Neutron imaging: Basics, techniques and applications. Springer (2022). https://doi.org/10.1007/978-981-16-6273-7
6. N. Kardjilov, I. Manke, R. Woracek et al., Advances in neutron imaging. Mater. Today **21**, 652–672 (2018). https://doi.org/10.1016/j.mattod.2018.03.001
7. J. Disch, L. Bohn, S. Koch et al., High-resolution neutron imaging of salt precipitation and transport in zero-gap CO_2 electrolysis. Nat. Commun. **13**, 6099 (2022). https://doi.org/10.1038/s41467-022-33694-y
8. N. Kardjilov, I. Manke, M. Strobl et al., Three-dimensional imaging of magnetic fields with polarized neutrons. Nat. Phys. **4**, 399–403 (2008). https://doi.org/10.1038/nphys912

9. M. Strobl, C. Grünzweig, A. Hilger et al., Neutron dark-field tomography. Phys. Rev. Lett. **101**, 123902 (2008). https://doi.org/10.1103/PhysRevLett.101.123902
10. R. Woracek, D. Penumadu, N. Kardjilov et al., 3D mapping of crystallographic phase distribution using energy-slective neutron tomography. Adv. Mater. **26**, 4069–4073 (2014). https://doi.org/10.1002/adma.201400192
11. R. Woracek, M. Krzyzagorski, H. Markötter et al., Spatially resolved time-of-flight neutron imaging using a scintillator CMOS-camera detector with kHz time resolution. Opt. Express **27**, 26218–26228 (2019). https://doi.org/10.1364/OE.27.026218
12. R.F. Ziesche, N. Kardjilov, W. Kockelmann et al., Neutron imaging of lithium batteries. Joule **6**, 35–52 (2022). https://doi.org/10.1016/j.joule.2021.12.007
13. X. Yuan, S.S. Han, Single-pixel neutron imaging with Artif Intell: Breaking the barrier in multi-parameter imaging, sensitivity, and spatial resolution. The Innovation **2**, 100100 (2021). https://doi.org/10.1016/j.xinn.2021.100100
14. S. Wang, C. Cao, W. Yin et al., A novel NDT scanning system based on line array fast neutron detector and DT neutron source. Materials **15**, 4946 (2022). https://doi.org/10.3390/ma15144946
15. A. Tengattini, N. Kardjilov, L. Helfen et al., Compact and versatile neutron imaging detector with sub-4 micrometer spatial resolution based on a single-crystal thin-film scintillator Opt. Express **30**, 14461–14477 (2022). https://doi.org/10.1364/OE.448932
16. Y.S. Song, J. Conner, X.D. Zhang et al., Monte Carlo simulation of a very high resolution thermal neutron detector composed of glass scintillator microfibers. Appl. Radiat. Isotopes. **108**, 100–107 (2016). https://doi.org/10.1016/j.apradiso.2015.12.035
17. H.Z. Bilheux, R. McGreevy, I.S. Anderson, Neutron imaging and applications: A reference for the imaging community. Springer (2009). https://doi.org/10.1007/978-0-387-78693-3
18. E.H. Lehmann, D. Mannes, M. Strobl et al., Improvement in the spatial resolution for imaging with fast neutrons. Nucl. Instrum. Meth. Sect. A **988**, 164809 (2021). https://doi.org/10.1016/j.nima.2020.164809
19. P. Trtik, J. Hovind, C. Grünzweig et al., Improving the spatial resolution of neutron imaging at Paul Scherrer Institut - The neutron microscope project. Physcs. Proc. **69**, 169–176 (2015). https://doi.org/10.1016/j.phpro.2015.07.024
20. D.Y. Li, S. Wang, H.Y. Huo et al., Design optimization and characterization of cold neutron imaging detector based on novel gadolinium scintillation glass fiber arrays and infinity corrected optics. IEEE T. Nucl. Sci. **69**, 2162–2167 (2022). https://doi.org/10.1109/TNS.2022.3208234
21. H.Y. Huo, H. Li, Y. Wu et al., Development of Cold Neutron Radiography Facility (CNRF) based on China Mianyang Research Reactor (CMRR). Nucl. Instrum. Meth. Sect. A **953**, 163063 (2020). https://doi.org/10.1016/j.nima.2019.163063
22. E.H. Lehmann, Basics of Neutron Imaging (2023). https://doi.org/10.5772/intechopen.110403
23. W. Wang, Q.H. Wang, Q. Yang et al., Experimental study of spatial resolution of MCPs for compact high-resolution neutron radiography system. Nucl. Instrum. Meth. Sec. A **1050**, 168179 (2023). https://doi.org/10.1016/j.nima.2023.168179
24. S. Han, M. Wu, H. Wang et al., Design of cold neutron imaging facility at China Advanced Research Reactor. Physcs. Proc. **43**, 73–78 (2013). https://doi.org/10.1016/j.phpro.2013.03.009
25. H. Li, S. Wang, C. Cao et al., Neutron imaging development at China Academy of Engineering Physics (CAEP). Physcs. Proc. **88**, 154–161 (2017). https://doi.org/10.1016/j.phpro.2017.06.021
26. Z.H. Wang, C. Dujardin, M.S. Freeman et al., Needs, trends, and advances in scintillators for radiographic imaging and tomography. IEEE T. Nucl. Sci. **70**, 1244–1280 (2023). https://doi.org/10.1109/TNS.2023.3290826
27. L.X. Zhang, S.Z. Chen, Z.D. Zhang et al., Resolution analysis of thermal neutron radiography based on accelerator-driven compact neutron source. Nucl. Sci. Tech. **34**, 76 (2023). https://doi.org/10.1007/s41365-023-01227-x
28. N. Kalyvas, P. Liaparinos, Analytical and Monte Carlo comparisons on the optical transport mechanisms of powder phosphors. Opt. Mater. **88**, 396–405 (2019). https://doi.org/10.1016/j.optmat.2018.12.006
29. X.F. Jiang, Q.L. Xiu, J.R. Zhou et al., Study on the neutron imaging detector with high spatial resolution at China spallation neutron source. Nucl. Eng. Technol. **53**, 1942–1946 (2021). https://doi.org/10.1016/j.net.2020.12.009
30. B. Winkler, Applications of neutron radiography and neutron tomography. Rev. Mineral. Geochem. **63**, 459–471 (2006). https://doi.org/10.2138/rmg.2006.63.17
31. Y.H. He, Y.Y. Huang, Z.R. Zeng et al., Single-pixel imaging with neutrons. Sci. Bull. **66**, 133–138 (2021). https://doi.org/10.1016/j.scib.2020.09.030
32. J.Y. Tang, Q. An, J.B. Bai et al., Back-n white neutron source at CSNS and its applications. Nucl. Sci. Tech. **32**, 1–10 (2021). https://doi.org/10.1007/s41365-021-00846-6
33. J.X. Zheng, Y. Zeng, J.J. Wang et al., Hydrogen-rich 2D halide perovskite scintillators for fast neutron radiography. J. Am. Chem. Soc. **143**, 21302–21311 (2021). https://doi.org/10.1021/jacs.1c08923
34. S.X. Wang, S.H. Deng, Z.J. Tan et al., The multifunctional neutron imaging system at GPPD: Design, principles and applications. Nucl. Instrum. Meth. Sect. A **1052**, 168315 (2023). https://doi.org/10.1016/j.nima.2023.168315
35. S. Koerner, E. Lehmann, P. Vontobel, Design and optimization of a CCD-neutron radiography detector. Nucl. Instrum. Meth. Sect. A **454**, 158–164 (2000). https://doi.org/10.1016/S0168-9002(00)00819-6
36. I. Mor, N. Eldad, M. Cohen et al., Development of a CCD based thermal neutron imaging detector for the Israeli Research Reactor IRR-1 at Soreq NRC. Nucl. Instrum. Meth. Sec. A **1012**, 165632 (2021). https://doi.org/10.1016/j.nima.2021.165632
37. Y. Liu, T.F. Zhu, Z. Luo et al., First-order primal-dual algorithm for sparse-view neutron computed tomography-based three-dimensional image reconstruction. Nucl. Sci. Tech. **34**, 118 (2023). https://doi.org/10.1007/s41365-023-01258-4
38. B. Tang, W. Yin, Q. Wang et al., High quantum efficiency rare-earth-doped Gd_2O_2S: Tb, F scintillators for cold neutron imaging. Molecules **28**, 1815 (2023). https://doi.org/10.3390/molecules28041815
39. L. Chen, Z. Bai, Q. Liu, Photoluminescence/cathodoluminescence properties and energy transfer mechanisms of fine-particle $Gd_2O_2S:Tb^{3+}$, RE^{3+} (RE = Dy, Eu) phosphor. J. Lumin. **267**, 120343 (2024). https://doi.org/10.1016/j.jlumin.2023.120343
40. O.H. Siegmund, J.V. Vallerga, A.S. Tremsin et al., High spatial resolution neutron sensing microchannel plate detectors. Nucl. Instrum. Meth. Sect. A **576**, 178–182 (2007). https://doi.org/10.1016/j.nima.2007.01.148
41. Y.H. Ma, H. Li, X. Yang et al., Wide energy region efficiency calibration study of a prompt gamma activation analysis facility. J. Radioanal. Nucl. Ch. **332**, 4009–4018 (2023). https://doi.org/10.1007/s10967-023-09097-8
42. Y.H. Ma, X. Yang, H.Y. Huo et al., Measurement study of neutron field relative distribution in sample for PGNAA based on NT. Nucl. Instrum. Meth. Sect. A **1045**, 167451 (2023). https://doi.org/10.1016/j.nima.2022.167451